Available online at www.sciencedirect.com
ScienceDirect
Journal of Computational Physics 227 (2008) 5799–5815
JOURNAL OF COMPUTATIONAL PHYSICS
www.elsevier.com/locate/jcp

A DGBGK scheme based on WENO limiters for viscous and inviscid flows

Guoxi Ni [a,*], Song Jiang [a], Kun Xu [b]

[a] LCP, Institute of Applied Physics and Computational Mathematics, P.O. Box 8009, Beijing 100088, China
[b] Department of Mathematics, Hong Kong University of Science and Technology, Clear Water Bay, Kowloon, Hong Kong

Received 14 September 2007; received in revised form 25 January 2008; accepted 11 February 2008
Available online 21 February 2008

Abstract

This paper presents a discontinuous Galerkin BGK (DGBGK) method for both viscous and inviscid flow simulations under a DG framework with a gas-kinetic flux and WENO limiters. In the DGBGK method, the construction of the flux in the DG method is based on the particle transport and collisional mechanism which not only couples the convective and dissipative terms together, but also includes both discontinuous and continuous terms in the flux formulation. Due to the connection between the gas-kinetic BGK model and the Euler as well as the Navier–Stokes equations, both viscous and inviscid flow equations can be simulated by a unified formulation. WENO limiters are used to obtain uniform high-order accuracy and sharp non-oscillatory shock transition. In the current method, the time accuracy is achieved by the direct integration of both time-dependent flux function at a cell interface and the flow variables inside each element. Numerical examples in one and two space dimensions are presented to illustrate the robustness and accuracy of the present scheme.

Keywords: DGBGK scheme; WENO limiters; Inviscid flows; Viscous flows; Taylor's expansion

1. Introduction

In hydrodynamic simulations, the finite volume (FV) and the discontinuous Galerkin (DG) finite element methods have been successfully developed and used in a wide range of applications. Most FV schemes use piecewise constant representation of flow variables inside each control volume and employ the reconstruction techniques to obtain high accuracy. Since a higher-order scheme usually uses a wider stencil than that in a lower-order scheme, difficulties emerge in its implementation in the flow computation on unstructured meshes with complex geometry. However, for the DG method, high-order accuracy is achieved by means of high-order polynomial approximation within each element rather than by means of wide stencils, where more information is stored and updated for each element in the computation. Because only neighboring elements interaction is included, the DG method becomes much easy and efficient in its application on unstructured meshes. The easy

* Corresponding author. Tel.: +86 10 62057509 2968; fax: +86 10 62057289.
E-mail addresses: gxni@iapcm.ac.cn (G. Ni), jiang@iapcm.ac.cn (S. Jiang), makxu@ust.hk (K. Xu).

0021-9991/$ - see front matter © 2008 Elsevier Inc. All rights reserved.
doi:10.1016/j.jcp.2008.02.009

handling of boundary condition is another benefit. Moreover, the use of discontinuous polynomial approximation produces a block diagonal mass matrix which becomes efficient to deal with numerically. At the same time, the slope limiting techniques can be incorporated in the DG method in a natural way. Explicit Runge–Kutta method is usually used for the time discretization in the DG method, which makes the resulting algorithm highly parallel. Now, the DG method has served as a high-order method for a broad class of problems, see, for example [6,9,7,8,10]. There is an extensive literature devoting to the study of the DG method for viscous and inviscid flows, such as [1,2,4,27,11].

For flows with strong discontinuities, the direct update of flow variables in the DG framework generates numerical oscillations. In order to get an oscillation-free solution, the limiting techniques used in the shock capturing upwind schemes were adopted here. In [23], the WENO limiters are successfully used in the DG method, where the main idea is to abandon the polynomial solution in the "troubled" cells and to reconstruct new polynomials with the information from neighboring cells. The use of the limiting techniques is the main reason for the success to capture shock discontinuities [16,12,14,20].

The gas-kinetic BGK scheme, proposed by Prendergast and Xu [22,28,29], is a finite volume method which makes use of the local integral solution of the collisional BGK model to compute a time-dependent gas distribution function at a cell interface and to obtain the numerical fluxes in the gas evolution stage. Since the BGK model is a statistical model, the particle transport and collision are coupled in the whole gas evolution process, and the particle collision time controls the physical dissipative coefficients in the macroscopic equations. Since the gas evolution is associated with a relaxation process, i.e., from a non-equilibrium state to an equilibrium one, the entropy condition is always satisfied by the BGK scheme. Based on the Chapman–Enskog expansion, from the gas-kinetic BGK model the Euler as well as the Navier–Stokes equations can be derived. In the smooth flow region, as the flow structure can be well resolved by the numerical cell size, the BGK scheme goes back to the Lax–Wendroff-type method for the compressible Navier–Stokes equations. In the discontinuity region, a delicate dissipative mechanism due to both kinematic and dynamic dissipation in the BGK scheme presents a stable and crisp shock transition, see [30,21]. Many engineering flow problems have been studied using the BGK scheme [17,18]. Another advantage to use the kinetic approach in the flux evaluation is due to the fact that the flux for the higher-order equations, such as Burnett and Super-Burnett, can be easily constructed [31]. Also, the physical modeling, such as gravity accelerating the particle movement or multicomponent gas interaction, can be easily implemented in the gas-kinetic formulation to design physically reliable schemes.

Hybrid schemes which inherit the merits of both the DG method and gas-kinetic schemes have been recently investigated by some authors. Based on the use of the collisionless Boltzmann equation, Tang and Warnecke proposed a gas-kinetic RKDG method for inviscid flows [25], where the accuracy and efficiency have been numerically demonstrated. Xu has proposed a DG-based BGK scheme for viscous fluids [32] for which a lower time integration method for the flow variables inside each cell was used. Recently, a Runge–Kutta DG–BGK scheme was presented for viscous fluids in [19] where a Runge–Kutta time discretization was used. For the schemes in [32,19] the usual TVD limiters have been employed.

In this paper, we shall incorporate the DG method with the BGK scheme to propose a DGBGK method for both inviscid and viscous flow simulations. In comparison with previous work, for the first time the following two recipes are presented. On the one hand, high-order time accuracy is obtained directly using a time-dependent flux function at a cell interface instead of implementing the Runge–Kutta or TVD–RK time discretization in the DG method [23,11]. Previously, a Runge–Kutta DG method incorporating with the BGK scheme was proposed in [19], and a lower-order time evolution method was used for the time integration inside each element in [32]. On the other hand, in the current paper the WENO limiters are successfully used in the DGBGK scheme, where both [32,19] used usual TVD limiter in the corresponding DG methods for viscous fluids.

The paper is organized as follows. Section 2 describes the DGBGK method. For the sake of simplicity, the detail algorithm is given only for one-dimensional formulation, and its extension to two-dimensional space is discussed briefly in Section 2.6. More specifically, Section 2.1 describes the relation between the BGK model and the compressible Euler as well as Navier–Stokes equations. Section 2.2 presents the formulation for the DG method. A brief description of construction of the BGK fluxes is given in Section 2.3. In Sections 2.4 and 2.5, the time discretization and the limiting procedure are presented. The performance of the proposed method

is illustrated in Section 3 through many numerical examples in both 1D and 2D cases. Finally, a brief comparison of the computational cost between the DGBGK scheme and the usual DG method with WENO limiters is presented.

2. A DGBGK scheme

Similar to many other finite volume methods, the gas-kinetic scheme is mainly about the flux evaluation at cell interfaces. The distinguishable feature of the gas-kinetic BGK scheme is that a Navier–Stokes flux is given directly from the MUSCL-type reconstructed initial data [15]. In the DG–WENO method, a high-order polynomial solution within each element is updated by using DG formulation and limited by using WENO limiters. In this section, we shall present a DGBGK scheme by incorporating the BGK flux into the above DG–WENO formulation. Firstly, we are going to present briefly the connection between the BGK model and macroscopic governing equations.

2.1. The BGK model and macroscopic equations

There are two approaches to describe flow motion. The first one is the macroscopic description, where the Euler and the Navier–Stokes equations are governing equations to describe the temporal and spatial evolution of the flow variables, i.e., mass, momentum and energy. Another description is based on the microscopic picture, where the gas-kinetic equation is used to describe the evolution of the particle distribution function.

Based on the gas-kinetic theory, the Euler and the Navier–Stokes system can be derived from a simplified Boltzmann equation, i.e. the Bhatnagar–Gross–Krook (BGK) model, through the Chapman–Enskog expansion [3,5]. In one space dimension, the BGK model can be written as

$$f_t + uf_x = \frac{g - f}{\tau}, \tag{2.1}$$

where f is the gas distribution function, g is the equilibrium state approached by f, u is the particle velocity, and τ is the particle collision time which is related to the viscosity and heat-conductivity coefficients. Both $f = f(x, t, u, \xi)$ and $g = g(x, t, u, \xi)$ are functions of x, t, u and the internal variable ξ.

Generally, the equilibrium state is a Maxwellian distribution with the form

$$g = \rho\left(\frac{\lambda}{\pi}\right)^{\frac{K+1}{2}} \mathrm{e}^{-\lambda[(U-u)^2+\xi^2]}, \tag{2.2}$$

where ρ and U are the macroscopic density and the velocity, respectively, λ is equal to $m/(2kT)$, m is the molecular mass, k is the Boltzmann constant and T is the temperature. The total number of degree of freedom K in ξ is equal to $(3-\gamma)/(\gamma-1)$, and ξ^2 denotes $\xi^2 = \xi_1^2 + \xi_2^2 + \cdots + \xi_K^2$.

The relation between the mass ρ, momentum ρU, energy E and the distribution function f is given by

$$(\rho, \rho U, E)^{\mathrm{T}} = \int \Psi f \,\mathrm{d}\Xi, \tag{2.3}$$

where

$$\Psi = (\psi_1, \psi_2, \psi_3)^{\mathrm{T}} = \left(1, u, \frac{1}{2}(u^2 + \xi^2)\right)^{\mathrm{T}},$$

and $\mathrm{d}\Xi = \mathrm{d}u\,\mathrm{d}\xi$ is the volume element in the phase space.

Since the mass, momentum, and energy are conservative during particle collisions, f and g satisfy the conservation constraint:

$$\int (g - f)\Psi \mathrm{d}\Xi = 0 \tag{2.4}$$

at any point in space and time.

For a local equilibrium state with $f = g$, the Euler system can be obtained by taking moments of Ψ to Eq. (2.1), and the corresponding Euler equations are

$$\begin{pmatrix} \rho \\ \rho U \\ E \end{pmatrix}_t + \begin{pmatrix} \rho U \\ \rho U^2 + P \\ (E+P)U \end{pmatrix}_x = 0, \tag{2.5}$$

where

$$E = \frac{1}{2}\rho\left(U^2 + \frac{K+1}{2\lambda}\right)$$

is the total energy and $P = \rho/(2\lambda)$ is the pressure, and the flux is computed from $\int ug\Psi \,\mathrm{d}\Xi$.

On the other hand, to the first-order of τ, the Chapman–Enskog expansion gives $f = g - \tau(g_t + ug_x)$, cf. [30]. Taking moments of Ψ to the BGK equation (2.1) with the above f, we get

$$\int (g_t + ug_x)\Psi \mathrm{d}\Xi = \tau \int (g_{tt} + 2ug_{xt} + u^2 g_{xx})\Psi \,\mathrm{d}\Xi, \tag{2.6}$$

from which the compressible Navier–Stokes equations with dynamic viscous coefficient $\mu = \tau P$ can be obtained,

$$\begin{pmatrix} \rho \\ \rho U \\ E \end{pmatrix}_t + \begin{pmatrix} \rho U \\ \rho U^2 + P \\ (E+P)U \end{pmatrix}_x = \begin{pmatrix} 0 \\ s_{1x} \\ s_{2x} \end{pmatrix}_x, \tag{2.7}$$

where

$$s_{1x} = \tau P\left[2\frac{\partial U}{\partial x} - \frac{2}{K+1}\frac{\partial U}{\partial x}\right], \quad s_{2x} = \tau P\left[\frac{2K}{K+1}U\frac{\partial U}{\partial x} + \frac{K+3}{4}\frac{\partial}{\partial x}\left(\frac{1}{\lambda}\right)\right]$$

are the viscous terms. Therefore, with different choices of the gas distribution function f, different macroscopic governing equations can be obtained.

2.2. DG spatial discretization

In this section, we will present a DG method for the Euler system (2.5) and the Navier–Stokes system (2.7) derived in the last subsection. For the sake of presentation, we first consider a one-dimensional scalar conservation law to illustrate the DG formulation,

$$\begin{cases} w_t + h(w)_x = 0, \\ w(x,0) = w_0(x), \quad x \in \mathbb{R}, \end{cases} \tag{2.8}$$

where $w, h \in \mathbb{R}$.

Let $\{I_i\}$ be computational cells on a computational domain I in $\mathbb{R}$. For a given cell $I_i = (x_{i-1/2}, x_{i+1/2})$, a semi-discrete DG method is obtained by multiplying (2.8) with a test function $v(x)$ as follows:

$$\frac{\mathrm{d}}{\mathrm{d}t}\int_{I_i} wv(x)\mathrm{d}x + \int_{\partial I_i} h(w)v(x)\mathrm{d}x - \int_{I_i} h(w)\partial_x v(x)\mathrm{d}x = 0,$$

where $v \in V^k$ and V^k is defined by

$$V^k := \{v \in L^1(I), v|_{I_i} \in p^k(I_i)\}$$

with $p^k(I_i)$ being the space of polynomials of degree at most k on I_i.

A Galerkin approximation solution $\tilde{w}(x,t)$ to w on I_i in the space V^k is constructed by

$$\tilde{w}(x,t) = \sum_{l=0}^{k} w_i^{(l)}(t)v_l^i(x), \tag{2.9}$$

where $\{v_l^i\}_1$ is a basis of $p^k(I_i)$. If we choose the Legendre polynomials to form a local orthogonal basis at x_i for $p^k(I_i)$, for example, in the one-dimensional case,

$$v_0^i(x) = 1, \quad v_1^i(x) = \left(\frac{x - x_i}{\Delta x_i}\right), \quad v_2^i(x) = \left(\frac{x - x_i}{\Delta x_i}\right)^2 - \frac{1}{12}, \ldots,$$

then we get the following system of ordinary differential equations

$$\frac{\mathrm{d}}{\mathrm{d}t} w_i^{(l)} + \frac{1}{\alpha_l}\left(\hat{h}(w_{i+1/2}^-, w_{i+1/2}^+) v_l^i(x_{i+1/2}) - \hat{h}(w_{i-1/2}^-, w_{i-1/2}^+) v_l^i(x_{i-1/2}) + \int_{I_i} \hat{h}(\tilde{w}(x,t)) \partial_x v_l^i(x) \mathrm{d}x\right) = 0, \tag{2.10}$$

where $l = 0, \ldots, k$, $w_{i+1/2}^{\pm} = \tilde{w}(x_{i+1/2}^{\pm}, t)$ are the left and right values of $\tilde{w}$ at a cell interface $x_{i+1/2}$, $\hat{h}(w_{i+1/2}^-, w_{i+1/2}^+)$ is the corresponding numerical flux at the cell interface $x_{i+1/2}$, and α_l $(l = 1, \ldots, k)$ are normalized constants $\alpha_l = \int_{I_i} |v_l^i|^2 \mathrm{d}x$.

A similar formulation can be obtained for the one-dimensional Euler system (2.5). With the expansions

$$\rho_i(x,t) = \sum_{l=0}^{k} \rho_i^{(l)}(t) v_l^i(x), (\rho U)_i(x,t) = \sum_{l=0}^{k} (\rho U)_i^{(l)}(t) v_1^i(x), E_i(x,t) = \sum_{l=0}^{k} E_i^{(l)}(t) v_1^i(x), \tag{2.11}$$

where ρ_i, $(\rho U)_i$ and E_i are the approximate solutions on the cell I_i. Here, $\rho_i^{(0)}$, $(\rho U)_i^{(0)}$ and $E_i^{(0)}$ are the cell-averaged values, $\rho_i^{(1)}, (\rho U)_i^{(1)}, E_i^{(1)}$ and $\rho_i^{(2)}, (\rho U)_i^{(2)}, E_i^{(2)}$ are the first- and second-order derivatives, respectively. Multiplying (2.5) by v_1^i, integrating by parts and replacing the conservative flow variables by (2.11), we get

$$\begin{cases} \frac{\mathrm{d}}{\mathrm{d}t}\rho_i^{(l)} + \frac{1}{\alpha_l}\{\hat{f}_\rho(x_{i+1/2},t) v_1^i(x_{i+1/2}) - \hat{f}_\rho(x_{i-1/2},t) v_1^i(x_{i-1/2}) - \int_{I_i} (\rho U)_i \partial_x v_1^i(x) \mathrm{d}x\} = 0, \\ \frac{\mathrm{d}}{\mathrm{d}t}(\rho U)_i^{(l)} + \frac{1}{\alpha_l}\{\hat{f}_{\rho U}(x_{i+1/2},t) v_1^i(x_{i+1/2}) - \hat{f}_{\rho U}(x_{i-1/2},t) v_1^i(x_{i-1/2}) - \int_{I_i} [(\rho U)_i U_i + P_i] \partial_x v_1^i(x) \mathrm{d}x\} = 0, \\ \frac{\mathrm{d}}{\mathrm{d}t} E_i^{(l)} + \frac{1}{\alpha_l}\{\hat{f}_E(x_{i+1/2},t) v_1^i(x_{i+1/2}) - \hat{f}_E(x_{i-1/2},t) v_1^i(x_{i-1/2}) - \int_{I_i} [(E_i + P_i) U_i] \partial_x v_1^i(x) \mathrm{d}x\} = 0, \end{cases} \tag{2.12}$$

where $U_i = (\rho U)_i/\rho_i$, $P_i = \frac{(\gamma-1)}{2}[2E_i - (\rho U)_i U_i]$, and $\hat{f}_\rho(x_{i+1/2},t)$, $\hat{f}_{\rho U}(x_{i+1/2},t)$ and $\hat{f}_E(x_{i+1/2},t)$ are the time-dependent numerical fluxes of the mass, momentum and energy at the cell interface $x_{i+1/2}$, respectively.

2.3. BGK numerical fluxes

In this sections, we will describe the BGK scheme for the calculation of numerical fluxes at a cell interface with the DG initial flow distributions.

The general solution f of (2.1) at any point x and time t is given by

$$f(x,t,u,\xi) = \frac{1}{\tau}\int_0^t g(x',t',u) \mathrm{e}^{-(t-t')/\tau} \mathrm{d}t' + \mathrm{e}^{-t/\tau} f_0(x - ut), \tag{2.13}$$

where $x' = x - u(t - t')$, and f_0 is the initial distribution function. In order to give the gas distribution function at the cell interface $x_{i+1/2}$, two unknowns g and f_0 in (2.13) have to be specified. Next, we show how to construct g and f_0.

Without loss of generality we may take $x_{j+1/2} = 0$. With the initial macroscopic flow states on both sides of a cell interface, to the Navier–Stokes order the initial gas distribution function f_0 is constructed as

$$f_0 = \begin{cases} g^{\mathrm{l}}[1 + a^{\mathrm{l}}x - \tau(a^{\mathrm{l}}u + A^{\mathrm{l}})], & x \leqslant 0, \\ g^{\mathrm{r}}[1 + a^{\mathrm{r}}x - \tau(a^{\mathrm{r}}u + A^{\mathrm{r}})], & x \geqslant 0, \end{cases} \tag{2.14}$$

where g^{l} and g^{r} are the Maxwellian distributions on the left- and right-hand sides of the cell interface $x = 0$ at $t = 0$, and have the unique correspondence with the initial macroscopic variables,

$$g^{\mathrm{l}} = g^{\mathrm{l}}(\mathbf{W}_{i+1/2}^{\mathrm{l}}) \quad \text{and} \quad g^{\mathrm{r}} = g^{\mathrm{r}}(\mathbf{W}_{i+1/2}^{\mathrm{r}}),$$

where

$$\mathbf{W}^{\mathrm{l,r}}_{i+1/2} = (\rho_i(x,t), (\rho U)_i(x,t), E_i(x,t))|_{(x=x^{\mathrm{l,r}}_{i+1/2}, t=0)}.$$

Therefore, g^{l} and g^{r} have been determined. The additional terms $-\tau g^{\mathrm{l}}(a^{\mathrm{l}}u + A^{\mathrm{l}})$ and $-\tau g^{\mathrm{r}}(a^{\mathrm{r}}u + A^{\mathrm{r}})$ in (2.14) are the non-equilibrium parts obtained from the Chapman–Enskog expansion of the BGK model, which take account for the dissipative effects. Note that f_0 and its spatial derivative are discontinuous at $x = 0$.

The coefficients $a^{\mathrm{l,r}}$, $A^{\mathrm{l,r}}$ in (2.14) are related to the derivatives of a Maxwellian distribution (cf. (2.2)) in space and time, which have the following form obtained from a Taylor expansion of the Maxwellian distribution:

$$a^{\mathrm{l}} = a^{\mathrm{l}}_1 + a^{\mathrm{l}}_2 u + \frac{1}{2}a^{\mathrm{l}}_3(u^2+\xi^2), \quad a^{\mathrm{r}} = a^{\mathrm{r}}_1 + a^{\mathrm{r}}_2 u + \frac{1}{2}a^{\mathrm{r}}_3(u^2+\xi^2), \tag{2.15}$$

$$A^{\mathrm{l}} = A^{\mathrm{l}}_1 + A^{\mathrm{l}}_2 u + \frac{1}{2}A^{\mathrm{l}}_3(u^2+\xi^2), \quad A^{\mathrm{r}} = A^{\mathrm{r}}_1 + A^{\mathrm{r}}_2 u + \frac{1}{2}A^{\mathrm{r}}_3(u^2+\xi^2). \tag{2.16}$$

Here $a^{\mathrm{l,r}}_j$ can be uniquely evaluated by taking the spatial derivative to (2.3) at $t = 0$ and using the spatial derivatives of the initial conservative flow variables $\rho_i(x,0)$, $(\rho U)_i(x,0)$, $E_i(x,0)$ at the left- and right-hand sides of the cell interface. Since the non-equilibrium parts have no contribution to the mass, momentum and energy conservation, the coefficients $A^{\mathrm{l,r}}_j$ in (2.16) can be also uniquely determined by the compatibility conditions:

$$\int \psi_i g^{\mathrm{l}}(a^{\mathrm{l}}u + A^{\mathrm{l}})\mathrm{d}\Xi = 0 \quad \text{and} \quad \int \psi_i g^{\mathrm{r}}(a^{\mathrm{r}}u + A^{\mathrm{r}})\mathrm{d}\Xi = 0, \quad i = 1,2,3. \tag{2.17}$$

Thus, we have now computed f_0 in (2.13). We point out here that even though the non-equilibrium parts have no contribution to the conservative flow variables (moments of Ψ), they do have contribution to the flux (moments of $u\Psi$).

To evaluate the equilibrium state g around $(x = 0, t = 0)$ in (2.13), we assume

$$g = g_0[1 + (1 - \mathrm{H}[x])\bar{a}^{\mathrm{l}}x + \mathrm{H}[x]\bar{a}^{\mathrm{r}}x + \overline{A}t], \tag{2.18}$$

where $\mathrm{H}[u]$ is the Heaviside function, and g_0 is a local Maxwellian distribution function located at $x = 0$. Note that g is continuous but has different slopes on both sides of $x = 0$.

Since g^{l} and g^{r} are already known, the flow variables $\mathbf{W}_0$ at the cell interface are computed as follows,

$$\mathbf{W}_0 = \int \Psi g_0 \,\mathrm{d}\Xi = \int_{u>0} \Psi g^{\mathrm{l}}\,\mathrm{d}\Xi + \int_{u<0} \Psi g^{\mathrm{r}}\,\mathrm{d}\Xi. \tag{2.19}$$

Consequently, g_0 can be determined from the above W_0.

The other coefficients, i.e., $\bar{a}^{\mathrm{l}}, \bar{a}^{\mathrm{r}}, \overline{A}$ in (2.18), have the following form obtained from Taylor's expansions of a Maxwellian distribution:

$$\bar{a}^{\mathrm{l}} = \bar{a}^{\mathrm{l}}_1 + \bar{a}^{\mathrm{l}}_2 u + \frac{\bar{a}^{\mathrm{l}}_3}{2}(u^2+\xi^2), \quad \bar{a}^{\mathrm{r}} = \bar{a}^{\mathrm{r}}_1 + \bar{a}^{\mathrm{r}}_2 u + \frac{\bar{a}^{\mathrm{r}}_3}{2}(u^2+\xi^2), \quad \overline{A} = \overline{A}_1 + \overline{A}_2 u + \frac{\overline{A}_3}{2}(u^2+\xi^2).$$

Their values are are evaluated as follows. In the discontinuous flow case, we use the following relation,

$$\frac{2(\mathbf{W}_0 - \overline{\mathbf{W}}_{\mathbf{i}})}{\Delta x_i} = \int \Psi g_0 \bar{a}^{\mathrm{l}}\,\mathrm{d}\Xi, \qquad \frac{2(\overline{\mathbf{W}}_{\mathbf{i+1}} - \mathbf{W}_{\mathbf{0}})}{\Delta x_i} = \int \Psi g_0 \bar{a}^{\mathrm{r}}\,\mathrm{d}\Xi$$

to get $\bar{a}^{\mathrm{l}}$ and $\bar{a}^{\mathrm{r}}$, where $\overline{\mathbf{W}}_\ell = (\rho^{(\mathbf{0})}_\ell, (\rho\mathbf{U})^{(\mathbf{0})}_\ell, \mathbf{E}^{(\mathbf{0})}_\ell)$ $(\ell = i, i+1)$ are the cell-averaged values of the conservative flow variables on the cells I_i and I_{i+1}, respectively. In the smooth flow case, we use the relation:

$$\int \Psi g_0 \bar{a}\,\mathrm{d}\Xi = \int_{u>0} \Psi g^{\mathrm{l}} a^{\mathrm{l}}\,\mathrm{d}\Xi + \int_{u<0} \Psi g^{\mathrm{r}} a^{\mathrm{r}}\,\mathrm{d}\Xi \tag{2.20}$$

to calculate a continuous derivative $\bar{a}^{\mathrm{l}} = \bar{a}^{\mathrm{r}} = \bar{a}$ of g. Since $\overline{A}$ is the only unknown in the representations (2.13) and (2.18) of f and g, we integrate the conservation constraint (2.4) in time,

$$\int_0^{\Delta t} \int (g - f)\Psi\,\mathrm{d}\Xi\,\mathrm{d}t = 0,$$

from which $\overline{A}$ can be evaluated uniquely.

Now, substituting (2.14) and (2.18) into (2.13), we obtain the gas distribution function f at the cell interface $x_{i+1/2}$ in the following form:

$$\begin{aligned} f(x_{i+1/2},t,u,\xi) &= (1-e^{-t/\tau})g_0 + \{\tau(-1+e^{-t/\tau}) + te^{-t/\tau}\}\{\bar{a}^{\mathrm{l}}H[u] + \bar{a}^{\mathrm{r}}(1-H[u])\}ug_0 \\ &\quad + \tau\left(\frac{t}{\tau} - 1 + e^{-t/\tau}\right)\overline{A}g_0 + e^{-t/\tau}\{(1-u(t+\tau)a^{\mathrm{l}})H[u]g^{\mathrm{l}} + (1-u(t+\tau)a^{\mathrm{r}})(1-H[u])g^{\mathrm{r}}\} \\ &\quad + e^{-t/\tau}\{-\tau A^{\mathrm{l}}H[u]g^{\mathrm{l}} - \tau A^{\mathrm{r}}(1-H[u])g^{\mathrm{r}}\}, \end{aligned} \tag{2.21}$$

With the above explicit representation of f, we can take moments of $u\Psi$ to f to obtain the time-dependent numerical fluxes $\hat{f}_\rho$, $\hat{f}_{\rho U}$, $\hat{f}_E$ across the cell interface $x_{i+1/2}$ in (2.12):

$$\begin{pmatrix} \hat{f}_\rho(x_{i+1/2},t) \\ \hat{f}_{\rho U}(x_{i+1/2},t) \\ \hat{f}_E(x_{i+1/2},t) \end{pmatrix} = \int uf(x_{i+1/2},t,u,\xi)\Psi \mathrm{d}\Xi. \tag{2.22}$$

Since the BGK flux includes both inviscid and viscous parts, the Euler and the Navier–Stokes fluxes can be obtained simultaneously by choosing appropriately the collision time τ. The DGBGK method does not require to evaluate the viscous part separately as other DG methods. For the simulation of the Euler equations we take τ as presented in (3.1), while for the compressible Navier–Stokes equations we take $\tau = 2\lambda/Re$, where Re is the Reynold number. It should be pointed out that it is well known that the BGK scheme corresponds to unit Prandtl number for viscous flows. However, one can easily fix the Prandtl number by modifying the heat flux [30].

2.4. Time discretization

In order to get a higher-order time accuracy, we have to deal with the time integration for the numerical fluxes at the cell interface and the volume integration in (2.12).

We make a direct time-integration to the time-dependent numerical fluxes $\hat{f}_\phi(x_{i+1/2},t)$ ($\phi = \rho, \rho U, E$) to get flow transport across the cell interface $x_{i+1/2}$,

$$\mathcal{F}^n_\phi(x_{i+1/2}) = \int_{t_n}^{t_{n+1}} \hat{f}_\phi(x_{i+1/2},t)\mathrm{d}t, \qquad \phi = \rho, \rho U, E. \tag{2.23}$$

The above integral can be evaluated explicitly. In other words, a time accurate numerical flux function $(\mathcal{F}^n_\rho, \mathcal{F}^n_{\rho U}, \mathcal{F}^n_E)^{\mathrm{T}}$ at $x_{i+1/2}$ is directly used.

For the time integration inside each element, we may use the Taylor's expansion up to the second-order to approximate the flow variations,

$$\begin{aligned} (\rho U)(x,t) &= (\rho U)(x,t_n) + (\rho U)_t(x,t_n)(t-t_n) + \mathrm{O}((\Delta t)^2), \\ (\rho U^2+P)(x,t) &= (\rho U^2+P)(x,t_n) + (\rho U^2+P)_t(x,t_n)(t-t_n) + \mathrm{O}((\Delta t)^2), \\ ((E+P)U)(x,t) &= ((E+P)U)(x,t_n) + ((E+P)U)_t(x,t_n)(t-t_n) + \mathrm{O}((\Delta t)^2). \end{aligned} \tag{2.24}$$

Based on Eq. (2.5), the temporal derivatives can be transferred to spatial derivatives,

$$\begin{aligned} (\rho U)_t(x,t_n) &= -(\rho U^2+P)_x, \\ (\rho U^2+P)_t(x,t_n) &= (1-\gamma)[(E+P)U]_x + \frac{\gamma-3}{2}[(\rho U^3)_x + 2UP_x], \\ [(E+P)U]_t(x,t_n) &= -\gamma U[(E+P)U]_x + (\gamma-1)U^2P_x + \frac{\gamma-1}{2}U(\rho U^3)_x - (E+P)(UU_x + P_x/\rho). \end{aligned} \tag{2.25}$$

Using (2.24) and (2.25) and integrating (2.12) with respect to t over the time interval (t_n, t_{n+1}), the following discrete DGBGK scheme for the Euler equations can be constructed,

$$
\begin{cases}
\rho_i^{(l),n+1} = \rho_i^{(l),n} - \frac{1}{\alpha_l}\left(\mathcal{F}_\rho^n(x_{i+1/2})v_1^i(x_{i+1/2}) - \mathcal{F}_\rho^n(x_{i-1/2})v_1^i(x_{i-1/2})\right) + \Delta t \int_{I_i}(\rho U)_i(x,t_n)\partial_x v_1^i(x)\mathrm{d}x \\
\qquad\qquad - \frac{(\Delta t)^2}{2}\int_{I_i}[(\rho U)_i U_i + P_i]_x(x,t_n)\partial_x v_1^i(x)\mathrm{d}x, \\
(\rho U)_i^{(l),n+1} = (\rho U)_i^{(l),n} - \frac{1}{\alpha_l}\left(\mathcal{F}_{\rho U}^n(x_{i+1/2})v_l^i(x_{i+1/2}) - \mathcal{F}_{\rho U}^n(x_{i-1/2})v_l^i(x_{i-1/2})\right) \\
\qquad\qquad + \Delta t\int_{I_i}[(\rho U)_i U_i + P_i](x,t_n)\partial_x v_l^i(x)\mathrm{d}x + \frac{(\Delta t)^2}{2}\int_{I_i}\{(1-\gamma)[(E_i+P_i)U_i]_x + \frac{\gamma-3}{2}[(\rho U)_i U_i^2]_x \\
\qquad\qquad + (\gamma-3)U_i\partial_x P_i\}(x,t_n)\partial_x v_1^i(x)\mathrm{d}x, \\
(E)_i^{(l),n+1} = E_i^{(l),n} - \frac{1}{\alpha_l}\left(\mathcal{F}_E^n(x_{i+1/2})v_l^i(x_{i+1/2}) - \mathcal{F}_E^n(x_{i-1/2})v_l^i(x_{i-1/2})\right) + \Delta t\int_{I_i}[(E_i+P_i)U_i](x,t_n)\partial_x v_l^i(x)\mathrm{d}x \\
\qquad\qquad - \frac{(\Delta t)^2}{2}\int_{I_i}\{\gamma U_i[(E_i+P_i)U_i]_x + (1-\gamma)U_i^2\partial_x P_i + \frac{1-\gamma}{2}U_i^3\partial_x(\rho U)_i \\
\qquad\qquad + (E_i+P_i)[U_i\partial_x U_i + \partial_x P_i/\rho_i]\}(x,t_n)\partial_x v_1^i(x)\mathrm{d}x,
\end{cases}
\tag{2.26}
$$

where U_i and P_i are the same as in (2.12).

In simulations, we use Gauss quadrature to compute the volume integrals on the right-hand side of (2.26), where the values of the approximate solution $(\rho_i, (\rho U)_i, E_i)$ at the Gaussian quadrature points are evaluated using (2.11). One can also use higher-order Taylor's expansions in the temporal variable for the terms in the volume integrals on the right-hand side of (2.12) to construct schemes of higher-order temporal accuracy.

We point out that instead of using the complicated expressions (2.25), one may take a simple approach to deal with the temporal derivative in (2.24) in computations, namely, to employ directly the backward difference to approximate the temporal derivative. Our numerical examples show that there is no essential difference in the numerical results between these two approaches.

2.5. WENO limiter

For the simulation of compressible inviscid flows using the DG method, the direct update of the numerical solutions will in general generate numerical oscillations across strong discontinuities. In this subsection, we use the WENO limiter proposed recently by Qiu and Shu [23] to eliminate spurious oscillations and enforce the stability.

There are two kinds of reconstruction for fluid dynamical systems: component-wise and characteristic-wise. In our numerical examples in Section 3, we use the characteristic-wise reconstruction for the two-dimensional tests and the component-wise reconstruction for the one-dimensional tests.

For simplicity, we describe the WENO reconstruction for the one-dimensional scalar Eq. (2.8). The reconstruction consists of two steps:

(1) First, to identify "troubled cells", namely those cells that need to be reconstructed.

Denote the cell interface values

$$w_{i+1/2}^- = w_i^0 + w_i^{\mathrm{r}}, \quad w_{i-1/2}^+ = w_i^0 - w_i^{\mathrm{l}}.$$

Based on (2.9), we will have

$$w_i^{\mathrm{r}} = \sum_{l=1}^{k} w_i^{(l)} v_1^i(x_{i+1/2}), \quad w_i^{\mathrm{l}} = -\sum_{l=1}^{k} w_i^{(l)} v_1^i(x_{i-1/2}).$$

Then, the standard minmod limiter is applied to the above values

$$w_i^{\mathrm{r(mod)}} = m(w_i^{\mathrm{r}}, w_{i+1}^{(0)} - w_i^{(0)}, w_i^{(0)} - w_{i-1}^{(0)}), \quad w_i^{\mathrm{l(mod)}} = m(w_i^{\mathrm{l}}, w_{i+1}^{(0)} - w_i^{(0)}, w_i^{(0)} - w_{i-1}^{(0)}),$$

where m is given by

$$m(\beta_1,\beta_2,\beta_3) = \begin{cases} s\ \min(|\beta_1|,|\beta_2|,|\beta_3|) & \text{if } s = \mathrm{sign}(a_1) = \mathrm{sign}(a_2) = \mathrm{sign}(a_3) \\ 0, & \text{otherwise,} \end{cases}$$

or by the TVB modified minmod function

$$\bar{m}(\beta_1,\beta_2,\beta_3)=\begin{cases}\beta_1 & \text{if } |\beta_1|\leqslant M\Delta x_i^2,\\ m(\beta_1,\beta_2,\beta_3) & \text{otherwise,}\end{cases}$$

where $M>0$ is a constant.
A cell is defined as a troubled cell if one of the minmod functions gets active (returns other than the first argument). Then, we mark this troubled cell for further reconstructions.

(2) To reconstruct the polynomial approximate solution in place of solution polynomial in each troubled cell while retaining its cell average. We reconstruct the degrees of freedom $w_i^{(l)}$ $(l=1,\ldots,k)$ in (2.9) for each troubled cell and retain only the cell average $w_i^{(0)}$. Here we do not want to repeat the process of Qiu and Shu's reconstruction, and refer to [23] for the details.

Now, for the compressible Euler and Navier–Stokes systems, in each troubled cell we reconstruct the degrees of freedom $\rho_i^{(l)},(\rho U)_i^{(l)},E_i^{(l)}$ $(l=1,\ldots,k)$ in (2.11) by the component-wise/characteristic-wise approach at each time step in the same manner as for the above $w_i^{(l)}$.

2.6. Extension to two spatial dimensions

In this section we briefly describe how to extend the previous constructed one-dimensional DGBGK scheme to the two-dimensional case. In two spatial dimensions, the DGBGK scheme is designed to solve the two-dimensional Euler or Navier–Stokes equations. The corresponding two-dimensional BGK model is

$$f_t+uf_x+vf_y=\frac{g-f}{\tau}, \tag{2.27}$$

where $f=f(x,y,t,u,v,\xi)$, and

$$g=\rho\left(\frac{\lambda}{\pi}\right)^{(K+2)/2}\mathrm{e}^{-\lambda[(u-U)^2+(v-V)^2+\xi^2]},$$

$K=(4-2\gamma)/(\gamma-1)$. Using the Chapman–Enskog expansion and taking moments of

$$\Psi=(1,u,v,(u^2+v^2+\xi^2)/2)^{\mathrm{T}}$$

to (2.27), one can get the macroscopic governing equations, which correspond to the two-dimensional Euler or Navier–Stokes system, see [29] for example. Since we use structured meshes for two-dimensional problems, we apply the dimensional splitting technique to construct the two-dimensional numerical fluxes by considering the BGK models

$$f_t+uf_x=\frac{g-f}{\tau}$$

in the x-direction and

$$f_t+vf_y=\frac{g-f}{\tau}$$

in the y-direction, respectively, and following a procedure similar to that in [19].

3. Numerical experiments

In order to validate the DGBGK scheme, we will present five numerical examples in this section. Three of them are the one-dimensional simulations and other two are two-dimensional flows.

3.1. Inviscid flows

For all the one-dimensional examples, the time step is taken as

$$\Delta t = \mathrm{CFL}\min_j \sqrt{|\Omega_j|}/(\max|U| + c), \tag{3.1}$$

where CFL is the CFL number, c is the sound speed, U is the fluid velocity and $|\Omega_j|$ is the volume of the domain Ω_j. In our numerical examples, the CFL number varies from 0.25 to 0.45.

For inviscid flows, the collision time τ is taken as

$$\tau = \epsilon\Delta t + \frac{|P_l - P_r|}{P_l + P_r}\Delta t,$$

where ϵ is a small parameter, P_l and P_r denote the pressure on the left- and right-hand sides of a cell interface. Here we take $\epsilon = 0.01$.

Example 1. Sod's shock-tube problem

The first test is the well-known Sod's shock-tube problem, which has been extensively studied [24]. It is a Riemann problem with two different constant states in a tube with unit length:

$$\begin{cases} (\rho, U, E) = (1.0, 0.0, 2.5), & 0.0 < x < 0.5, \\ (\rho, U, E) = (0.125, 0, 0.25), & 0.5 < x < 1.0. \end{cases}$$

This Riemann problem has the exact solution, which can be easily found in text books. The computation is carried out on a uniform mesh with 400 cells. The numerical results obtained by the DGBGK scheme are shown in Figs. 1–4, where the constant M in the WENO limiter is chosen to be $M = 0.01$. Figs. 1 and 2 are the contours of the computed density by the third-order and the second-order DGBGK schemes in comparison with the exact solution, respectively. The corresponding numerical results for the velocity are presented in Figs. 3 and 4. From Figs. 1–4 we see that the numerical results obtained using both the third- and second-order schemes are very close to the exact solution, and the third-order scheme performs obviously better than the second-order one.

Example 2. Shu–Osher's entropy wave interaction case

This is a typical example of shock interaction with entropy waves, see [13]. A Mach 3 moving shock wave interacts with sine density wave, i.e.,

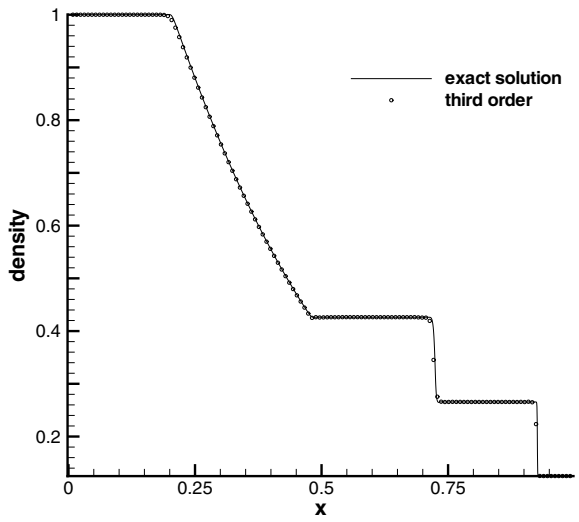

Fig. 1. Sod's shock-tube problem. Density distribution by the third-order DGBGK scheme with 400 cells.

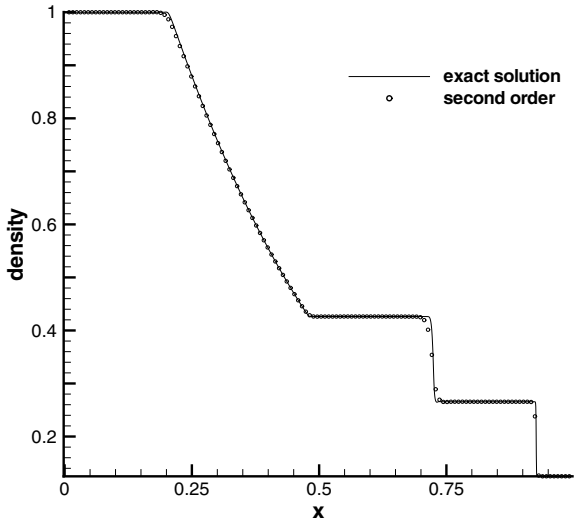

Fig. 2. Sod's shock-tube problem. Density distributions by the second-order DGBGK scheme with 400 cells.

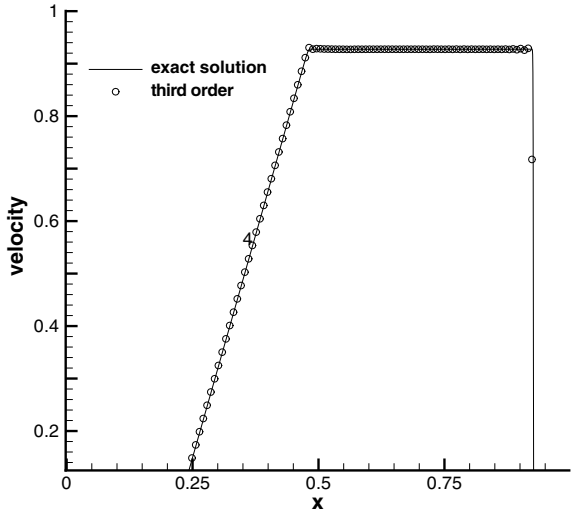

Fig. 3. Sod's shock-tube problem. Velocity distributions by the third-order DGBGK scheme with 400 cells.

$$\begin{cases} (\rho, U, P) = (3.857143, 2.629369, 10, 333333), & 0.0 < x < 5.0, \\ (\rho, U, P) = (1 + \epsilon \sin(5x), 0, 1), & 5.0 < x < 10.0, \end{cases}$$

where $\epsilon = 0.2$. To our knowledge, this problem has no exact solution, but does have a numerical "exact" solution computed using the fifth-order finite difference WENO scheme with 2000 cells [23]. In the computation here we use 400 cells and choose the constant M in the WENO limiter to be $M = 0.01$. The density contours obtained using the second- and third-order DGBGK schemes are presented in Figs. 5 and 6, which are compared with the "exact" solution. We see again that the third-order scheme is obviously more accurate than the second-order one. We also observe that the computed result by the third-order DGBGK scheme is better than that by the fourth-order scheme in [23].

In order to test the accuracy of the scheme, in Table 1 we present the L^1 error and numerical order of the scheme, which is obtained by extracting the data at the computational region $5.80 < x < 7.68$ in the current test case. In this region, the solution is basically smooth even though it is strongly effected by the shock front.

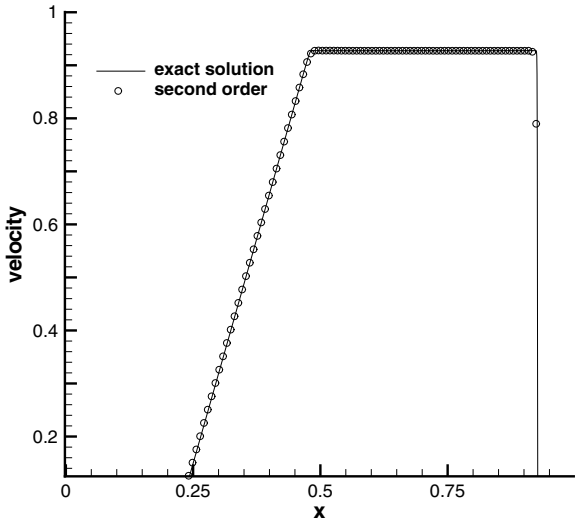

Fig. 4. Sod's shock-tube problem. Velocity distributions by the second-order DGBGK scheme with 400 cells.

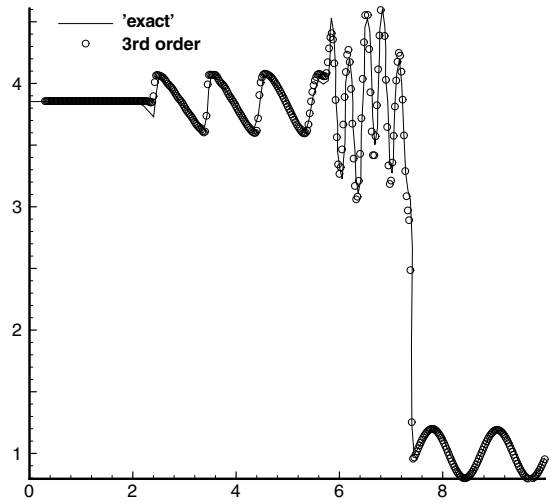

Fig. 5. Shock and sound wave interaction. Density distribution by the third-order DGBGK scheme with 400 cells.

Table 1
Accuracy results for entropy wave

p^1 case			p^2 case		
N	L^1 error	Order	N	L^1 error	Order
40	13.6474		40	4.2359	
80	1.7228	2.98	80	1.0749	1.96
160	1.0388	0.73	160	0.8719	0.84
320	0.3884	1.42	320	0.2156	2.05
640	0.1174	1.73	640	0.0355	2.61

The L^1 error and numerical order at $t = 1.92$ on the domain $5.80 < x < 7.68$.

From Table 1, we can roughly see the second- and third-order accuracy from p^1 and p^2 DGBGK schemes with WENO limiters. Since the smooth solution passes through the shock discontinuity, the order estimate can be

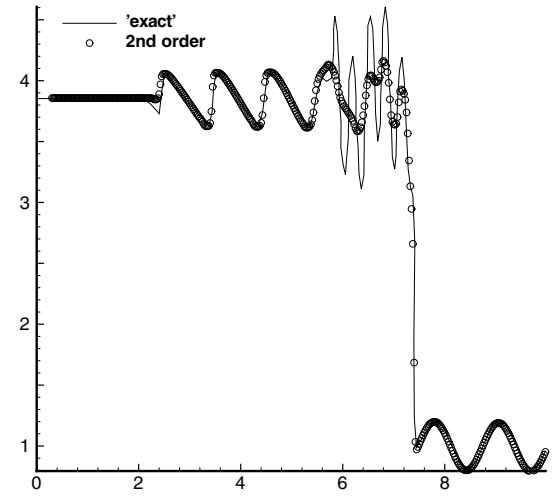

Fig. 6. Shock and sound wave interaction. Density distribution by the second-order DGBGK scheme with 400 cells.

only considered as an approximation. For the test case without shocks, as presented in the early publications, the current DGBGK scheme can certainly get the theoretical order of accuracy.

Example 3. Blast wave interaction

In this example, we consider the interaction of blast waves, see [26,13]. The initial data are

$$\begin{cases} (\rho, U, P) = (1, 0, 1000), & 0.0 < x < 1.0, \\ (\rho, U, P) = (1, 0, 0.01), & 1.0 < x < 9.0, \\ (\rho, U, P) = (1, 0, 100), & 9.0 < x < 10.0. \end{cases}$$

A reflecting boundary condition is applied to both ends. This problem has a numerical "exact" solution computed by using the fifth-order finite difference WENO scheme with 2000 cells [23]. The computation is carried out using the WENO limiter with $M = 0.01$ on a uniform mesh with 400 grid points. The computed density contours by the second- and third-order DGBGK schemes are shown in Figs. 7 and 8 and they are compared

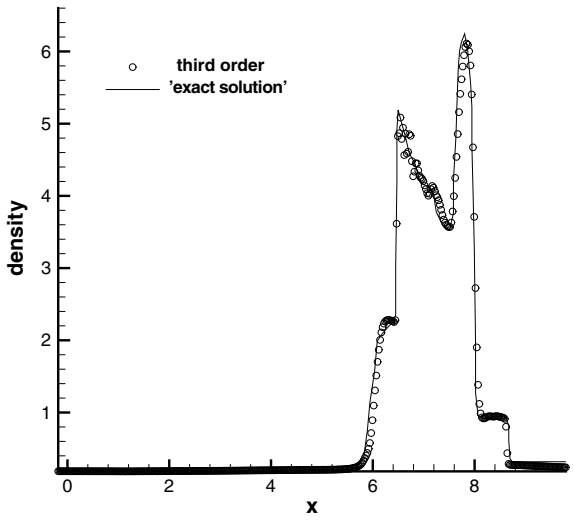

Fig. 7. Blast wave interaction. Density distribution obtained by the third-order DGBGK scheme with 400 cells.

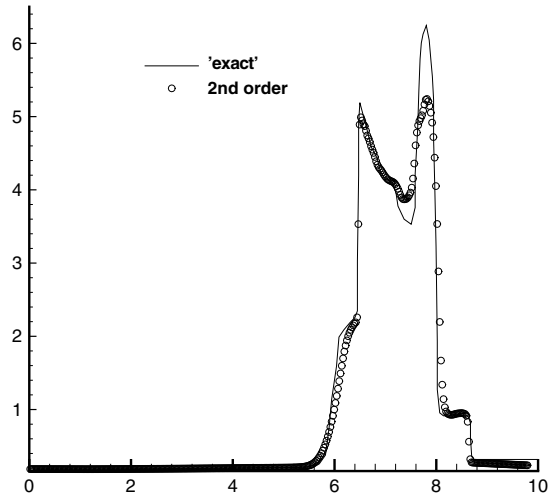

Fig. 8. Blast wave interaction. Density distribution obtained by the second-order DGBGK scheme with 400 cells.

with the "exact" solution. Again, we observe that the third-order scheme performs apparently much better than the second-order one, and the result obtained by the third-order DGBGK scheme is comparable with the fourth-order scheme in [23].

Example 4. Double Mach Reflection

This problem has been extensively studied by Woodward and Colella [26] and by many others. A schematic description of computational set-up can be found in [26]. Here we use exactly the same set-up as in [26]. Namely, a Mach 10 shock hits a 60° wedge, and the computational domain is $(0,4) \times (0,1)$. The undisturbed air ahead of the shock has a density of 1.4 and a pressure of 1, a uniform 360×120 cells are used. In Fig. 9 we

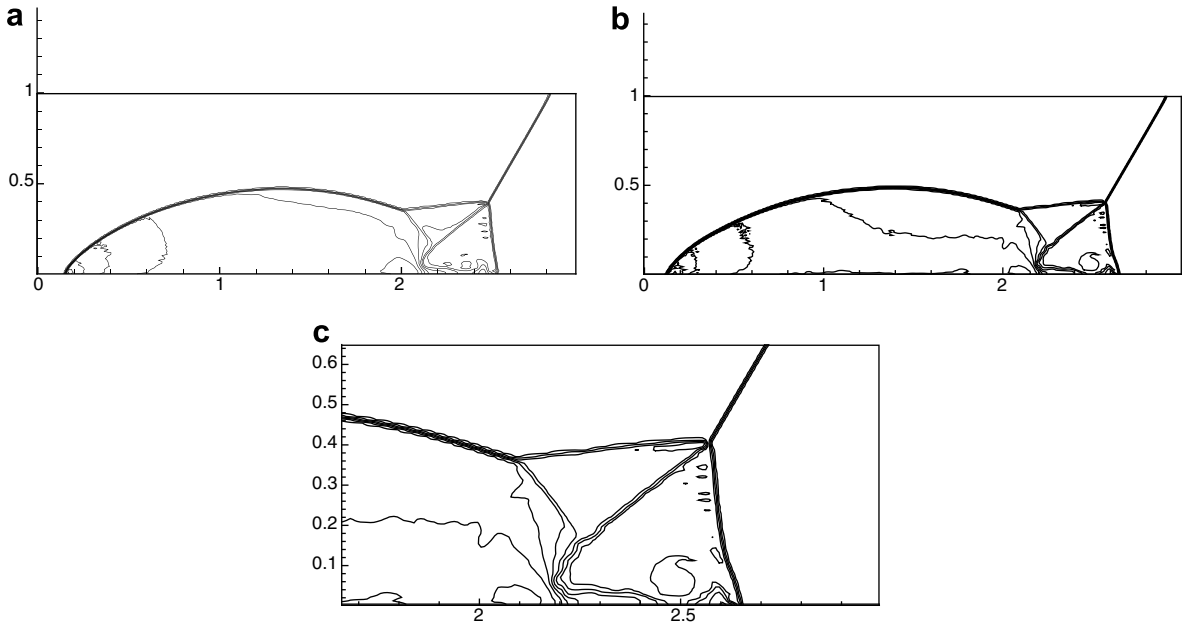

Fig. 9. Mach reflection: (a) Density contours computed using the second-order DGBGK scheme. (b) Density contours computed using the third-order DGBGK scheme. (c) Local density distribution around the triple point computed using the third-order DGBGK scheme.

give two density contours in (a) for the p^1 case and in (b) for the p^2 case. Obviously, the numerical results here reproduce those in [26,23].

3.2. Viscous flows

In this section we present a two-dimensional viscous flow problem to validate our scheme. From Section 2.1 we understand that the compressible Navier–Stokes equations can be recovered by taking moments of Ψ to (2.2) when f is expanded up to the first-order of the Chapman–Enskog expansion. For viscous flows, we take the collision time $\tau = 2\lambda/Re$, where Re is the Reynolds number. We point out that although the BGK scheme gives unit Prandtl number for viscous flows, which can be easily fixed by modifying the heat flux.

Example 5. Laminar boundary layer

This example is the laminar boundary layer over a flat plate with length L. Here we solve the compressible Navier–Stokes equations (2.7) indirectly. In the computation the Mach number is $M = 0.2$ and the Reynolds number based on the upstream flow state and the length L is $Re = 10^5$. A uniform rectangular grid with 480×120 cells is used on the computational domain $(0,4) \times (0,1)$.

The contour plot of the x-direction velocity U computed by the second-order DGBGK scheme is shown in (c) of Fig. 10. The computed velocity U at the location $x = 1.5$ by the third- and second-order DGBGK schemes is shown in Fig. 10a and b, where the Blasius solution is also presented for comparison. In the plots, η is equal to $y\sqrt{U_\infty/(\nu x)}$ and ν is the viscosity coefficient. Fig. 10 shows that the numerical solutions obtained by both second- and third-order schemes are in good agreement with the exact solution.

As the end of this section we remark on the computational cost between the current DGBGK scheme and the RKDG method with WENO limiters presented in [23]. For the double Mach reflection test and with the computer *Centrino Duo* with 1.66 GHZ speed and 512 MB memory, the DGBGK scheme used 46 h to finish the computation, while for the RKDG method with the same WENO limiters it took 25 h. However, even for

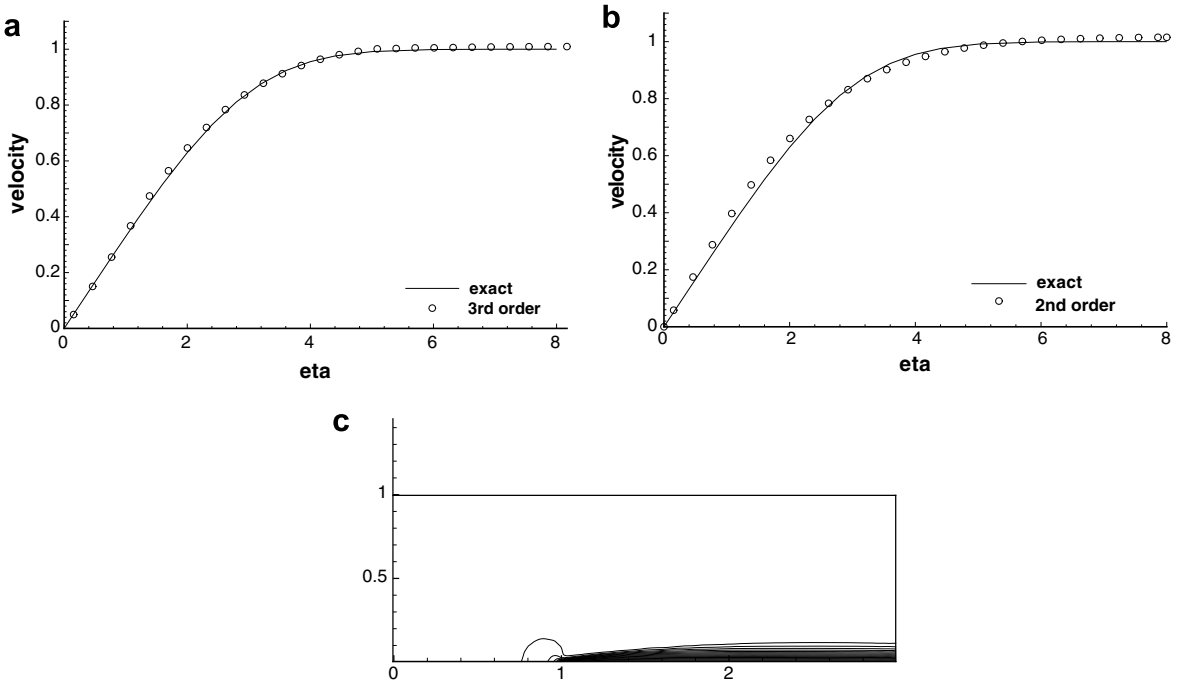

Fig. 10. Laminar boundary layer. (a) Computed velocity distribution by the third-order DGBGK scheme at $x = 1.5$. (b) Numerical solution obtained using the second-order DGBGK scheme. (c) Contours of the velocity obtained by the second-order scheme.

the inviscid flow calculation, the DGBGK method is always solving the viscous flow equations. For the RKDG method, the Euler equations are actually solved. With the above consideration, we can safely say that the DGBGK method is slightly more expensive than the RKDG one. For both methods, almost 30,000 cells, or 70% of total cells, need to be reconstructed at each time step. The reconstruction for troubled cells is computationally expensive. How to design an efficient limiter is an urgent problem facing all DG developers.

4. Conclusion

A DGBGK scheme has been developed for both viscous and inviscid flow simulations using a DG framework with a gas-kinetic flux and WENO limiters. The new scheme inherits some merits of both the DG and the BGK methods. The construction of the flux in the DGBGK scheme is based on the particle transport and collisional mechanism which not only couples the convective and dissipative terms, but also includes both discontinuous and continuous flow distributions in the flux evaluation at cell interfaces. Due to the relation between the gas-kinetic BGK model and the Euler as well as the Navier–Stokes equations, both viscous and inviscid flow equations can be solved by a unified scheme. WENO limiters have been used to obtain uniform high-order accuracy and sharp non-oscillatory shock transition. In the current DGBGK scheme, the time accuracy has been obtained by direct integration of both the time-dependent flux function at the cell interface and the flow variables inside each element. For the volume integration, a Lax–Wendroff-type expansion is used to achieve high-order time accuracy. Numerical examples in one and two space dimensions illustrate the robustness and accuracy of the current DGBGK scheme. We have also compared the computational cost of the current DGBGK scheme with the RKDG method with WENO limiters. The comparison indicates that the current scheme is slightly expensive than the RKDG method for viscous flow. A lot of computational time has been spent on the limiting process. How to get rid of or design an efficient limiter is an important question to be answered.

Acknowledgement

This work was supported by the National Basic Research Program (No. 2005CB321700), NSFC (Grant No. 10225105), and by a grant of Chinese Academy of Engineering Physics (No. 20060644). K. Xu was supported by Hong Kong Research Grant Council through RGC HKUST621005 and 621406.

References

[1] F. Bassi, S. Rebay, A high-order accurate discontinuous finite element method for the numerical solution of the compressible Navier–Stokes equations, J. Comput. Phys. 131 (1997) 267.
[2] F. Bassi, S. Rebay, An implicit high-order discontinuous Galerkin method for the steady state compressible Navier–Stokes equations, Computational Fluid Dynamics'98, Proceedings of the Fourth European Computational Fluid Dynamics Conference, vol. 2, 1998, p. 1226.
[3] P.L. Bhatnagar, E.P. Gross, M. Krook, A model for collision processes in gases I: small amplitude processes in charged and neutral one-component systems, Phys. Rev. 94 (1954) 511.
[4] C.E. Baumann, J.T. Oden, A discontinuous hp finite element method for the Euler and Navier–Stokes equations, Int. J. Numer. Meth. Fluids 31 (1999) 79.
[5] S. Chapman, T.G. Cowling, The Mathematical Theory of Non-Uniform Gases, Cambridge University Press, 1990.
[6] B. Cockburn, G.E. Karniadakis, C.W. Shu, The development of discontinuous Galerkin methods, in: B. Cockburn, G.E. Karniadakis, C.W. Shu (Eds.), Discontinuous Galerkin Methods: Theory, Computation and Applications, Springer, Berlin, 2000.
[7] B. Cockburn, S.Y. Lin, C.W. Shu, TVB Runge–Kutta local projection discontinuous Galerkin finite element method for conservation laws III: one-dimensional systems, J. Comput. Phys. 84 (1989) 90.
[8] B. Cockburn, S. Hou, C.W. Shu, TVB Runge–Kutta local projection discontinuous Galerkin finite element method for conservation laws IV: the multidimensional case, Math. Comput. 54 (1990) 545.
[9] B. Cockburn, C.W. Shu, TVB Runge–Kutta local projection discontinuous Galerkin finite element method for scalar conservation laws II: general framework, Math. Comput. 52 (1989) 411.
[10] B. Cockburn, C.W. Shu, The Runge–Kutta discontinuous Galerkin method for conservation laws V: multidimensional systems, J. Comput. Phys. 141 (1998) 199.
[11] B. Cockburn, C.W. Shu, Runge–Kutta discontinuous Galerkin method for convection-dominated problems, J. Sci. Comput. 16 (2001) 173.

[12] B. Costa, W.S. Don, D. Gottlieb, R. Sendersky, Two-dimensional multi-domain hybrid spectral-WENO methods for conservation laws, Commun. Comput. Phys. 1 (2006) 548.
[13] G.S. Jiang, C.W. Shu, Efficient implementation of weighted ENO schemes, J. Comput. Phys. 126 (1996) 202.
[14] A. Kurganov, C.T. Lin, On the reduction of numerical dissipation in central-upwind schemes, Commun. Comput. Phys. 2 (2007) 141.
[15] B. van Leer, Towards the ultimate conservative difference scheme IV. A new approach to numerical convection, J. Comput. Phys. 23 (1977) 276.
[16] B. van Leer, Upwind and high-resolution methods for compressible flow: from donor cell to residual-distribution schemes, Commun. Comput. Phys. 1 (2006) 192.
[17] G. May, A. Jameson, Unstructured algorithm for the inviscid and viscous flows embedded in a unified solver architecture: Flo3xx. AIAA Paper 2005-0318, 2005.
[18] G. May, B. Srinivasan, A. Jameson, An improved gas kinetic BGK finite volume method for three-dimensional transonic flow, J. Comput. Phys. 220 (2007) 856.
[19] H.W. Liu, K. Xu, A Runge–Kutta discontinuous Galerkin method for viscous flow equations, J. Comput. Phys. 224 (2007) 1223.
[20] Y. Liu, C.W. Shu, E. Tadmor, M. Zhang, Non-oscillatory hierarchical reconstruction for central and finite volume schemes, Commun. Comput. Phys. 2 (2007) 933.
[21] T. Ohwada, On the construction of kinetic schemes, J. Comput. Phys. 177 (2002) 156.
[22] K.H. Prendergast, K. Xu, Numerical hydrodynamics from gas kinetic theory, J. Comput. Phys. 109 (1993) 53.
[23] J. Qiu, C.W. Shu, Runge–Kutta discontinuous Galerkin method using WENO limiter, SIAM J. Sci. Comput. 26 (3) (2005) 907.
[24] G.A. Sod, A survey of several finite difference methods for system of nonlinear hyperbolic conservation law, J. Comput. Phys. 27 (1978) 1.
[25] H.Z. Tang, G. Warnecke, A Runge–Kutta discontinuous Galerkin method for the Euler equations, Comput. Fluids 34 (2005) 375.
[26] P. Woodward, P. Colella, The numerical simulation of two-dimensional fluids with strong shock, J. Comput. Phys. 54 (1984) 115.
[27] Y. Xing, C.W. Shu, A new approach of high order well-balanced finite volume WENO schemes and discontinuous Galerkin methods for a class of hyperbolic systems with source terms, Commun. Comput. Phys. 1 (2006) 100.
[28] K. Xu, K.H. Prendergast, Numerical Navier–Stokes solutions from gas kinetic theory, J. Comput. Phys. 114 (1994) 9.
[29] K. Xu, Gas-kinetic Schemes for Unsteady Compressible Flow Simulations. VKI for Fluid Dynamics Lecture Series 1998-03, 1998.
[30] K. Xu, A gas-kinetic BGK scheme for the Navier–Stokes equations and its connection with artificial dissipation and Godunov method, J. Comput. Phys. 171 (2001) 289.
[31] K. Xu, Super-Burnett solutions for Poiseuille flow, Phys. Fluids 15 (2003) 2077.
[32] K. Xu, Discontinuous Galerkin BGK method for viscous flow equations: one-dimensional systems, SIAM J. Sci. Comput. 23 (2004) 1941.